



## Supplementary Materials for

### **Scalable, Phase-inverted, Hierarchically Porous Polymers for Passive Daytime Radiative Cooling**

**Authors: J. Mandal, Y. Fu, A. Overvig, K. Sun, M. Jia, N. Shi, H. Zhou, X.Xiao, N. Yu\*, Y. Yang\***

Correspondence to: Email: [yy2664@columbia.edu](mailto:yy2664@columbia.edu) (Y. Y.), [ny2214@columbia.edu](mailto:ny2214@columbia.edu) (N. Y.)

#### **This PDF file includes:**

Materials and Methods (Section 1)  
Supplementary Text (Section 2-13) with  
Figs. S1 to S16  
Tables S1 to S3

## Section 1. Materials and Methods

*Making the hierarchically porous poly(vinylidene-co-hexafluoropropene) P(VdF-HFP) coatings:* P(VdF-HFP) (Kynar Flex 2801) from Arkema was first dissolved in acetone, and then had water added to make a P(VdF-HFP)-acetone-water precursor solution with a 1:8:1 mass ratio. The precursor solution was then painted, spray-coated, drop-cast or dip-cast onto different substrates to achieve the desired coating thicknesses. Freestanding sheets were obtained by peeling the coatings off smooth surfaces (e.g. Al foil). As described in Section 13, precursor solutions were also made for other polymers, like poly(methyl-methacrylate) and used to make coatings.

*Optical characterization:* Spectral reflectance of the P(VdF-HFP)<sub>HP</sub> coatings was determined separately in the ultraviolet (0.35-0.41  $\mu\text{m}$ ), visible to near-infrared (0.41-1.05  $\mu\text{m}$ ) and near-infrared to mid-infrared (1.06-14  $\mu\text{m}$ ) wavelength ranges. For the first range, measurement was taken using a Fourier-transform-based Spectrometer (Vertex 80, Bruker) equipped with a Xenon plasma light source (Energetiq eq-99) and an integrating sphere (Model IS200, Thorlabs). For the second range, measurements were taken with the same integrating sphere, and at specific wavelengths from a high-power supercontinuum laser (SuperK Extreme, NKT Photonics) coupled to a tunable filter (Fianium LLTF contrast). For the third range, a Fourier Transform Infrared (FT-IR) spectrometer (Vertex 70v, Bruker) and a gold integrating sphere (Model 4P-GPS-020-SL, Labsphere), along with a mercury cadmium telluride detector were similarly used. For the 0.35-1  $\mu\text{m}$  wavelengths, a pristine, calibrated diffuse reflector (Item SM05CP2C, Thorlabs) was used as a reference, while for larger wavelengths, gold-coated Al foils were used. Angular measurements were taken with the P(VdF-HFP)<sub>HP</sub> samples placed inside the integrating spheres at different angles to intercept the incident light. Additional measurements of reflectance between 0.3-0.4  $\mu\text{m}$  and 14-19  $\mu\text{m}$  were taken using similar setups. Specular reflectance measurements from 5-25  $\mu\text{m}$  was taken using the ellipsometer described below. The reflectance spectra were patched, and  $\bar{R}_{\text{solar}}$  and  $\bar{\epsilon}_{\text{LWIR}}$  calculated from the patches using Equations S1 and 2 in Section 2. Transmission spectra were likewise measured, with the samples placed at the mouth of the integrating sphere.

*Refractive index measurements:* refractive index measurements were taken for solid blocks of P(VdF-HFP) using J.W. Woollam V-VASE and IR-VASE ellipsometers.

*Imaging and microscopy:* Images of the P(VdF-HFP)<sub>HP</sub> samples were taken using Nikon D3300 (visible) and FLIR T640 (LWIR) cameras. Scanning electron microscopy was done using a Zeiss Sigma VP scanning electron microscope (SEM).

*Simulations:* Please refer to Section 6

*Cooling power and sub-ambient temperature demonstrations:* Please refer to Section 8.

*Aging and Exposure Tests:* Please refer to Section 12.

*Addition of color:* to add color to the white P(VdF-HFP)<sub>HP</sub> coatings, food colors (Brilliant Blue and Yellow 5) were added to the 1:8:1 precursor solution in different ratios to get blue, yellow and black coatings. Spectral reflectances of drop-cast coatings of the solutions on black substrates were then measured to demonstrate their high NIR-to-SWIR reflectance.

*Synchrotron Characterizations:* The tomography measurement (microCT) was done at 2BM Beamline of Advanced Photon Source at Argonne National Laboratory. The X-ray energy was 40keV, and the detector was PCI.EDGE5.5, coupled with 23  $\mu\text{m}$  thick GGG:Eu scintillator and 10x Mitutoyo long working distance lens; detector effective pixel size was 0.65 x 0.65  $\mu\text{m}$ . Tomography data reconstruction was done with Tomopy, an open source tomographic data processing package developed at Advanced Photon Source. Pore structure was thresholded and segmented from the tomographic reconstructed data, and the pore analysis was done with ImageJ '3D Objects Counter' plugin. Ultra-small Angle X-Ray Scattering (USAXS) characterizations were performed at the beamline 9-ID-C at the Advanced Photon Source (APS) at Argonne National Laboratory. The X-ray beam was at 12 keV energy and had a profile of 1.5 mm (H) x 0.8 mm (V). The complete USAXS data collection used an advanced-design Bonse-Hart camera (USAXS) with integrated fixed length SAXS (500 mm) and WAXS (300 mm) cameras. USAXS data reduction and curve fitting was done using the Igor-pro based Irena software toolbox.

## Section 2. Definition of Solar Reflectance, Thermal Emittance and Cooling Power of PDRC coatings

To achieve passive daytime radiative cooling, an object must minimize radiative heat gain from the sun and maximize radiative heat loss to the cold sky above. The first implies that the surface must have a high angular solar reflectance  $\bar{R}_{solar}(\theta)$ , defined as:

$$\bar{R}_{solar}(\theta) = \frac{\int_0^\infty I_{solar}(\lambda) \cdot R_{solar}(\theta, \lambda) d\lambda}{\int_0^\infty I_{solar}(\lambda) d\lambda} \quad (S1)$$

where  $\theta$  is the angle of incidence from the surface normal,  $\lambda$  is the wavelength,  $I_{solar}(\lambda)$  is the ASTM G173 Global solar intensity spectrum, and  $R_{solar}(\theta, \lambda)$  is the surface's angular spectral reflectance. Given that  $\bar{R}_{solar}(\theta)$  of P(VdF-HFP) is measured to be quite uniform across angles (Fig. 1E), the hemispherical solar reflectance  $\bar{R}_{solar}$  is only marginally different from  $\bar{R}_{solar}(\theta)$ . Therefore, in this paper, they are assumed to be equivalent.

To maximize thermal emission into the sky, the surface must have a high hemispherical LWIR emittance  $\bar{\epsilon}_{LWIR}$ , defined as:

$$\bar{\epsilon}_{LWIR} = \frac{\int_{8\mu m}^{13\mu m} I_{BB}(T, \lambda) \cdot \epsilon(T, \lambda) d\lambda}{\int_{8\mu m}^{13\mu m} I_{BB}(T, \lambda) d\lambda} \quad (S2)$$

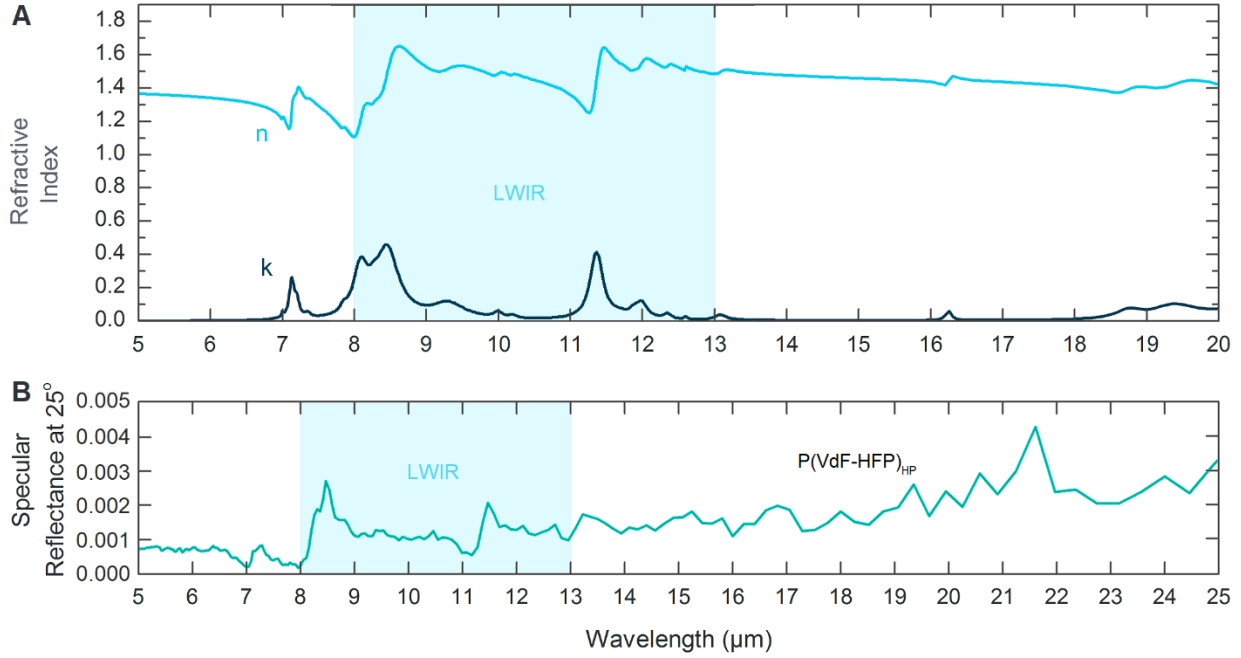
where the 8-13  $\mu m$  bounds represent the LWIR atmospheric transmittance window,  $I_{BB}(T, \lambda)$  is the spectral intensity emitted by a blackbody at temperature  $T$  (assumed to be 25°C, unless otherwise stated) and  $\epsilon(T, \lambda)$  is the surface's spectral hemispherical thermal emittance. The angular LWIR emittance  $\bar{\epsilon}_{LWIR}(\theta)$  can be similarly defined from  $\epsilon(T, \lambda, \theta)$ . With a sufficiently high  $\bar{R}_{solar}(\theta)$  and  $\bar{\epsilon}_{LWIR}$ , the surface can minimize net radiative heat gain from the environment, or even achieve a net radiative heat loss or 'cooling power'.

For our study, we assume a model where radiative heat transfer between the P(VdF-HFP)<sub>HP</sub> and the sky occurs only in the solar (0.35-2.5  $\mu m$ ) and part of the mid-to-far Infrared wavelengths (4-20  $\mu m$ ). The P(VdF-HFP)<sub>HP</sub> coating is assumed to be horizontal on the ground, unless otherwise stated. For such a situation, the cooling power is as follows:

$$P_{cooling} = -(1 - \bar{R}_{solar}(\theta)) \times I_{solar}(\theta) + \int_{4\mu m}^{20\mu m} \int \epsilon(\Omega, \lambda) \times (I_{BB}(T_{coating}, \lambda) - I_{sky}(\Omega, \lambda)) d\Omega d\lambda \quad (S3)$$

where  $\bar{R}_{solar}(\theta)$  is the directional solar reflectance of the coating,  $I_{solar}(\theta)$  is the global solar intensity for an incidence angle  $\theta$ ,  $\epsilon(\Omega, \lambda)$  is the spectral, directional emittance of the P(VdF-HFP)<sub>HP</sub> coating,  $\Omega$  is the solid angle,  $T_{coating}$  is the temperature of the P(VdF-HFP)<sub>HP</sub> coating,  $I_{BB}(T_{coating}, \lambda)$  is the theoretical maximum (blackbody) spectral emission from the coating and  $I_{sky}(\Omega, \lambda)$  is the sky's spectral, directional radiance. It should be noted that almost all of the radiative heat loss occurs through the LWIR (Tables S1 and S2) atmospheric transmission window, making  $\bar{\epsilon}_{LWIR}$  a sufficient indicator of performance. Regardless, for the calculations, presented in Sections 8 and 9, we opt for the 4-20  $\mu m$  wavelength range, and use Equation S3. It should be

noted that integrating sphere measurements of spectral emittance  $\epsilon(\lambda)$  were accurate only up till  $\lambda \sim 19 \mu\text{m}$ . Beyond that,  $\epsilon(\lambda)$  was assumed to be the same as  $\epsilon(\lambda = 19 \mu\text{m})$  up to  $\lambda = 20 \mu\text{m}$ . This is a reasonable approximation for two reasons. Firstly, P(VdF-HFP) has an intrinsic emission peak at  $\lambda \sim 19.5 \mu\text{m}$  (Fig. S1A). Secondly, specular reflectance  $R(\lambda, 25^\circ)$  measurements, which is a qualitative indicator of diffuse reflectance, show little change between 19 and 20  $\mu\text{m}$  (Fig. S1B).

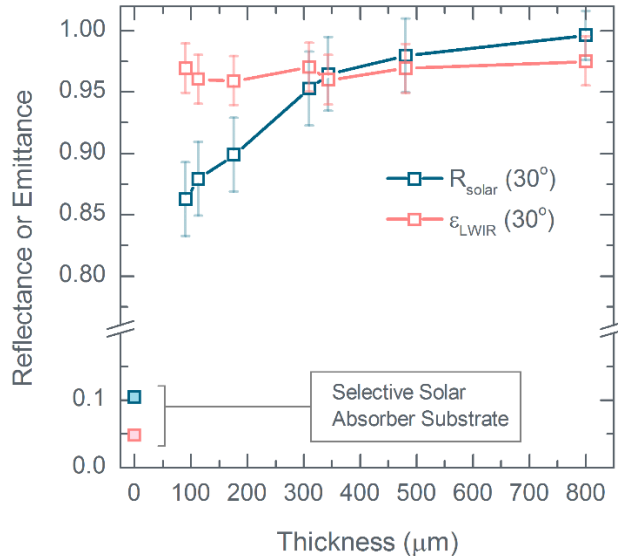


**Figure S1.** (A) The refractive index of P(VdF-HFP), showing emission peaks in the 16, 18.7 and 19.5  $\mu\text{m}$  wavelengths beyond the LWIR window. (B) Directional reflectance  $R(\lambda, 25^\circ)$ , showing comparable values beyond the LWIR window up to 25  $\mu\text{m}$  wavelength, relative to the LWIR values.

### Section 3. $\bar{R}_{solar}$ and $\bar{\epsilon}_{LWIR}$ vs P(VdF-HFP)<sub>HP</sub> Coating Thickness

Fig. S2 shows measured  $\bar{R}_{solar}$  and  $\bar{\epsilon}_{LWIR}$  of the P(VdF-HFP)<sub>HP</sub> coatings as a function of the thickness. Evidently, a 90  $\mu\text{m}$  thickness is sufficient to yield a high  $\bar{\epsilon}_{LWIR} > 0.95$ , beyond which the emittance varies little. This suggests that even for small thicknesses, the porous structure of the P(VdF-HFP)<sub>HP</sub> is enough to augment the intrinsic emittance of the P(VdF-HFP) to a high value. Solar reflectance, however, has a more pronounced trend, with a thickness of  $\sim 300 \mu\text{m}$  needed for  $\bar{R}_{solar}$  to exceed 0.95, and  $\sim 480 \mu\text{m}$  needed to reach 0.98. The increase in solar reflectance with thickness likely arises from the increased back-scattering of light from the thicker, non-absorptive, porous polymer layer. As thickness increases even further (e.g. to  $\sim 800 \mu\text{m}$ ), the reflectance approaches 1.00. An example of the spectral reflectance for this remarkably high performance is shown in Fig. S15.

Notably, the above performances are achieved on a selective solar absorber ( $\bar{R}_{solar} \sim 0.1$  and  $\bar{\epsilon}_{LWIR} \sim 0.05$ ) (17), which the optical opposite of a PDRC coating. Other surfaces, such as metals and typical black or white coatings have one or both of  $\bar{R}_{solar}$  and  $\bar{\epsilon}_{LWIR}$  favorable for PDRC. Therefore, the values in Fig. S2 represent a lower bound of performance with respect to the choice of substrate, making the performance substrate-independent in this sense. It is also noteworthy that due to the  $\sim 50\%$  porosity of P(VdF-HFP)<sub>HP</sub> coatings, all the thicknesses stated here are effectively half of the measured value with respect to the amount of material. Furthermore, the measured thicknesses themselves are considerably less than those of high-performance cool roof coatings, which often need to be close to 1 mm in thickness (30). While PDRC designs reported recently in the literature show good optical performances ( $\bar{R}_{solar} > 0.95$  and  $\bar{\epsilon}_{LWIR} > 0.6$ ) with thinner films (5-8), they are sophisticated and rely on silver to reflect sunlight. Additionally, the large thicknesses required for durable rooftop coatings make their thinness unessential.



**Figure S2.** Variation of  $\bar{R}_{solar}$  and  $\bar{\epsilon}_{LWIR}$  of the P(VdF-HFP)<sub>HP</sub> coatings with thickness. Error bars indicate the uncertainty in  $\bar{R}_{solar}$  and  $\bar{\epsilon}_{LWIR}$  due to errors associated with integrating sphere measurements and sample-to-sample variation. The measurements were taken at a  $30^\circ$  angle of incidence.

## Section 4. Transmittance Measurements and Mean free path Calculations

To gain a better understanding of the structure of P(VdF-HFP)<sub>HP</sub> and the behavior of sunlight incident on it, we experimentally extract the photon mean free path ( $l_f$ ) based on a diffusion theory (31), which relates the transmittance ( $T$ ) of a P(VdF-HFP)<sub>HP</sub> sheet to its thickness ( $L$ ) by the following relation:

$$T = \frac{1+z_e}{\frac{L}{l_f} + 2z_e} \quad (\text{S4})$$

Where  $z_e$ , the extrapolation length ratio, is a sample-dependent number on the order of unity, and is related to the transmittance as a function of the angle ( $\theta$ ) from the surface normal.  $z_e$  is calculated from the angular probability distribution of transmitted light as follows:

$$\frac{P(\mu)}{\mu} = \frac{z_e + \mu}{\frac{z_e}{2} + \frac{1}{3}} \quad (\text{S5})$$

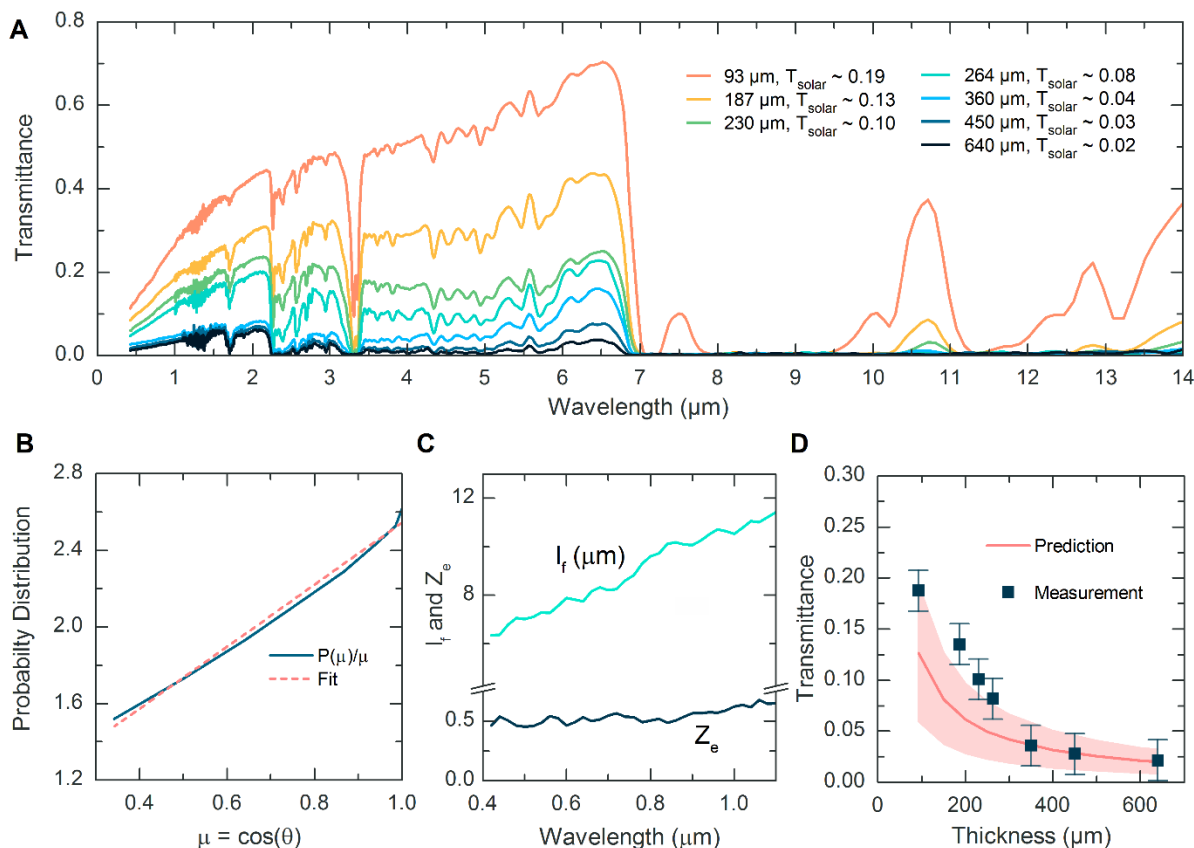
where  $\mu = \cos(\theta)$ , and  $\int P(\theta) \sin \theta d\theta = \int P(\mu) d\mu = 1$ .

We first measure the spectral transmittance  $T(\lambda)$  of P(VdF-HFP)<sub>HP</sub> sheets, which shows an expected decrease with sheet thickness (Fig. S3A). Then, we measure the angular profile  $P(\theta)$  of the transmitted light, using a 360  $\mu\text{m}$  thick sample. The sample is first affixed to the center of rotation of a rotation stage, and then illuminated by the supercontinuum-laser-and-filter system described in Section 1. On an arm attached to the rotation stage, an aspheric lens (25.4 mm in diameter) is placed 100 mm away from the sample. A silicon photodiode is placed facing the sample, and at the focal plane of the lens (20 mm further from the center of rotation). The lens-detector system is rotated in increments of 10 degrees, and at each angle the spectral transmittance is measured. The values are then normalized such that  $\int P(\theta) \sin \theta d\theta = 1$ .

From the angular transmittance measurements, the extrapolation length is calculated using Equation S5. A linear regression is used to extract  $z_e$  for each wavelength, and the fit aligns well with experimental data (Fig. S3B). The value of  $z_e$ , roughly  $\sim 0.5$ , agrees with results in the literature (31), and is nearly constant with illuminating wavelength as expected (31). Finally, the photon mean free path,  $l_f$ , is extracted by entering the known values of  $L$  (360  $\mu\text{m}$ ) and  $z_e$  into Equation S4.

Fig. S3C depicts the calculated  $z_e$  and  $l_f$  values in the wavelength range of 420 – 1100 nm, which contains 72% of sunlight, and for which the required optical setup was available. The values of  $l_f$ , which lie between 6-12  $\mu\text{m}$  for the measured wavelengths hint at the interaction between different wavelengths of light and the hierarchical porous P(VdF-HFP). For example, the blue wavelengths, which would be efficiently scattered by the nanoporous features, have  $l_f \sim 6 \mu\text{m}$ , which is close to the mean size of the micropores. This implies that blue wavelengths are primarily scattered at the nanoporous boundaries between the micropores (Fig. S4). Longer wavelengths ( $\sim 1 \mu\text{m}$ ), on the other hand, have  $l_f \sim 12 \mu\text{m}$ , implying that they are less well-scattered by the nanoporous boundaries, and penetrate deeper into the P(VdF-HFP)<sub>HP</sub> before the combined scattering by nano

and micropores leads to substantial reflection. This is evident in the transmission spectra for thin P(VdF-HFP)<sub>HP</sub> sheets in Fig. S3A, which show a higher transmission for longer solar wavelengths.



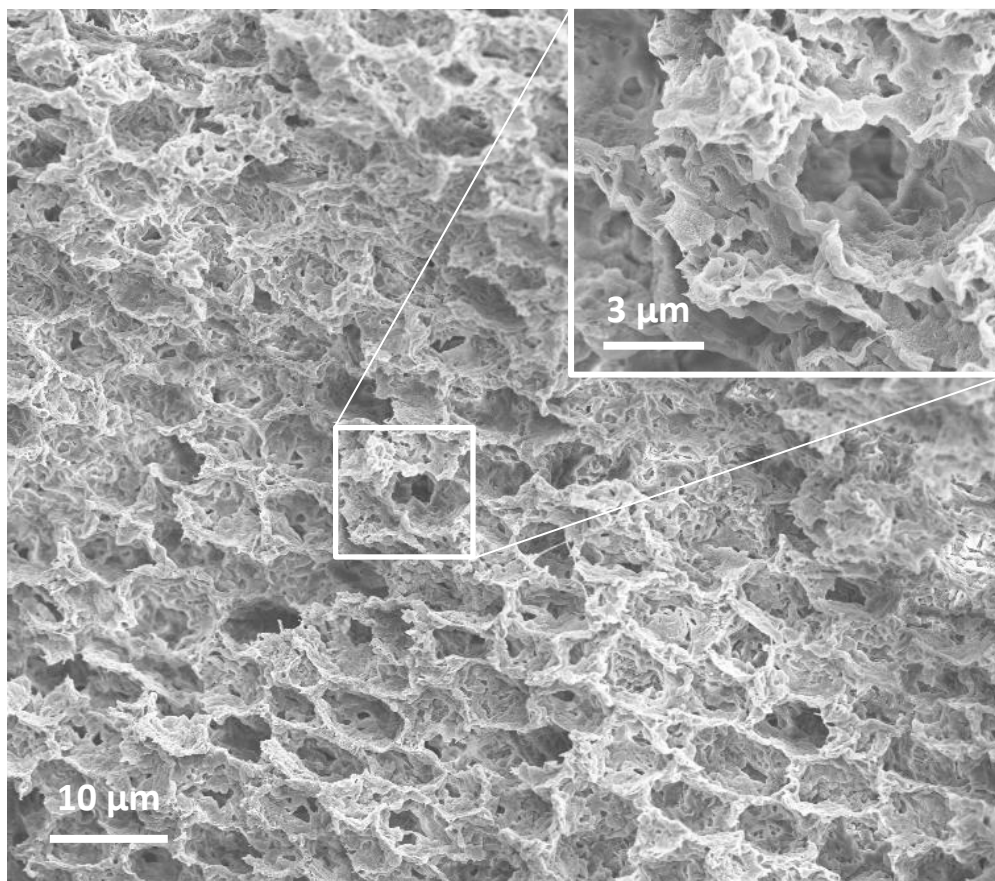
**Figure S3.** (A) Spectral transmittance of different thicknesses of P(VdF-HFP)<sub>HP</sub> sheets. Solar transmittances are stated in the legend. As expected, transmittance drops with increasing thickness for the solar wavelengths, and at thicknesses beyond 187 μm, the LWIR transmittance becomes negligible. (B) Graph of  $P(\mu)/\mu$  vs  $\mu$ . (C) Calculated extrapolation length ratio  $z_e$  and mean-free path  $l_f$  for  $\lambda = 0.42$ - $1.1$  μm. (D) Measured and predicted values (corresponding to  $z_e \sim 0.55$  and  $l_f \sim 8.2$  μm) of  $T(\lambda = 720 \text{ nm})$ . Shaded region indicates the upper and lower bounds (corresponding to  $l_f \sim 13.3$  μm and  $3.7$  μm) of the predicted transmittance arising from uncertainties in  $T$  ( $0.035 \pm 0.02$ ) of the sample.

Using the calculated  $z_e$  and  $l_f$  for  $\lambda = 0.72$  μm (above/below which 50% of solar intensity lies), Equation S4 is used to predict the transmittance as a function of sheet thickness, which is shown alongside measured values in Fig. S3D. As shown, the predicted values are in agreement with the measured values for P(VdF-HFP)<sub>HP</sub> thicknesses  $> 300$  μm. At low thicknesses, the predicted model shows lower transmittances compared to the measured values. The difference points to a lower diffuse scattering in thinner samples. This could be due to morphological differences between thinner and thicker sheets, as the speed of solvent evaporation during phase inversion is dependent on the film thickness, and can influence morphology (32). Regardless, the above characterization provides key physical insights into the optical property of P(VdF-HFP)<sub>HP</sub>. Furthermore, the excellent agreement for thicknesses  $> 300$  μm used in our paper corroborate that high opacities leading to substrate-independent optical performance are indeed achievable.



## Section 5. Morphology of P(VdF-HFP)<sub>HP</sub> Coatings and Effect of P(VdF-HFP):Water Ratio

The phase inversion process imparts a hierarchically porous structure on P(VdF-HFP)<sub>HP</sub>. As shown in Fig. S4, the P(VdF-HFP)<sub>HP</sub> films contain large micropores with sizes between 2-10  $\mu\text{m}$ , with the boundaries between the micropores made up of a nanoporous phase (Fig. S4 Inset). The hierarchical porosity is quantified by measurements performed on micrographs of P(VdF-HFP)<sub>HP</sub>, which appears to show a bimodal pore size distribution (Fig. 2C and S7D-F). Nanopores between 0.05-1  $\mu\text{m}$  are measured to have a mean diameter of  $\sim 0.2 \mu\text{m}$ , and micropores are measured to have a mean diameter  $\sim 5.5 \mu\text{m}$ . Pores  $< 50 \text{ nm}$  in size scatter little sunlight, so they are not considered in our SEM analysis.

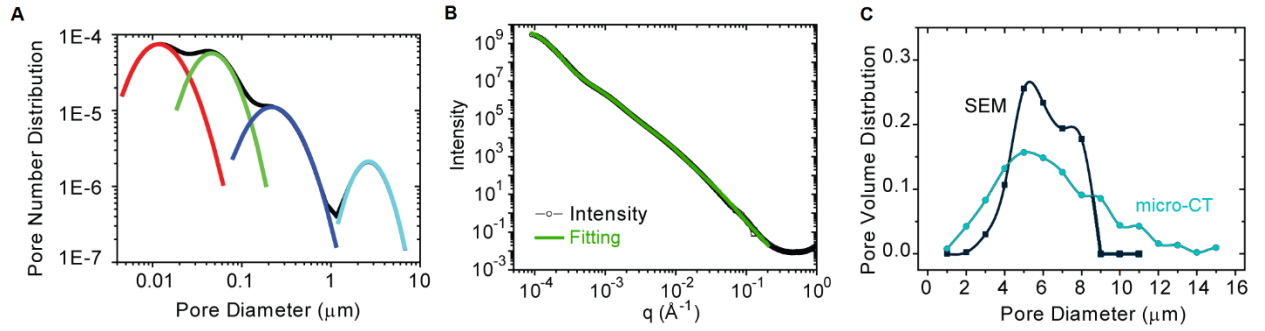


**Figure S4.** SEM micrograph of a cross-section of P(VdF-HFP)<sub>HP</sub>, showing micropores with sizes  $\sim 5 \mu\text{m}$ . The inset contains a magnified view of the center, showing the nanoporous P(VdF-HFP) which make up the micropore walls.

The size distribution measurements are corroborated by ultra-small-angle X-ray scattering (USAXS) measurements and microcomputed tomography (micro-CT) scans of the P(VdF-HFP)<sub>HP</sub>. As shown in Fig. S5A, the USAXS measurements confirm the hierarchical porous structure, with multimodal pore size distribution peaks observed at  $\sim 0.3 \mu\text{m}$  and  $\sim 3 \mu\text{m}$ . Peaks at  $\sim 0.01$  and  $\sim 0.05 \mu\text{m}$  is also observed. However, such pores are too small for their scattering to be significant, and are classified collectively with the larger,  $\sim 0.1 \mu\text{m}$  nanopores. The total number of nanopores  $< 1 \mu\text{m}$  in size appear to be greater than the number of micropores by a factor of  $\sim 10^2$ .

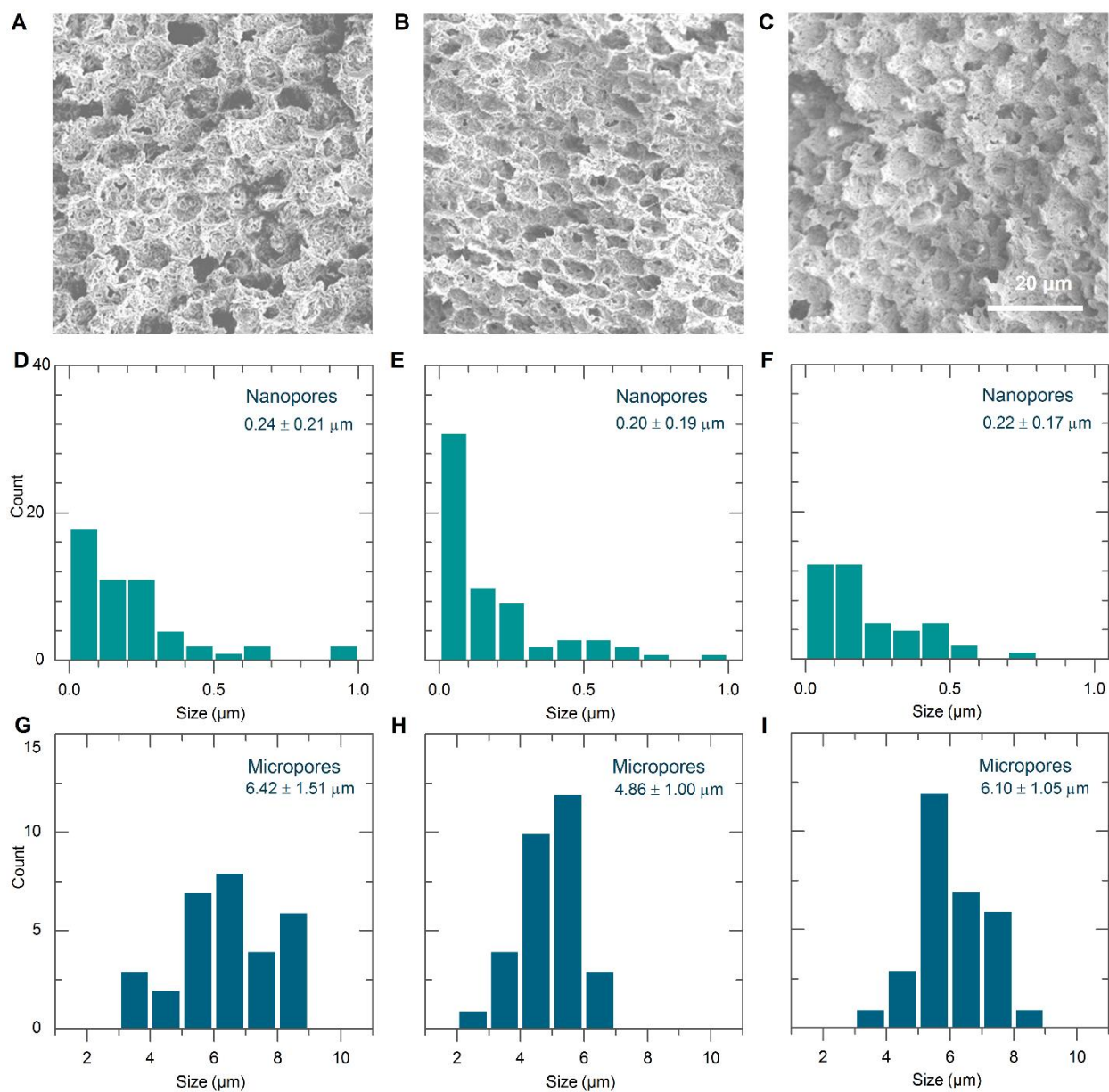
However, since the minimum  $q$  in USAXS is  $9 \times 10^{-5} \text{ \AA}^{-1}$ , corresponding to maximum size of  $\pi/q = 3.5 \text{ \mu m}$ , the size distribution and peak for pores  $> 1 \text{ \mu m}$  are only semiquantitative. Therefore, we do not quantify the relative abundance of micro and nanopores, and present their SEM size distributions separately (Figs. 2C, S6 and S7).

Micro-CT measurements in Fig. S5C show a similar pore volume peak ( $\sim 5 \text{ \mu m}$ ) to the SEM characterizations. The differences observed at small ( $< 4 \text{ \mu m}$ ) and large ( $> 9 \text{ \mu m}$ ) pore sizes are likely due to the low resolution ( $0.65 \text{ \mu m}$ ) of the micro-CT scanner, whose Boolean pixelation can overestimate the thicknesses of the nanoporous walls and underestimate pore size, or not register thin nanoporous walls and overestimate pore size.



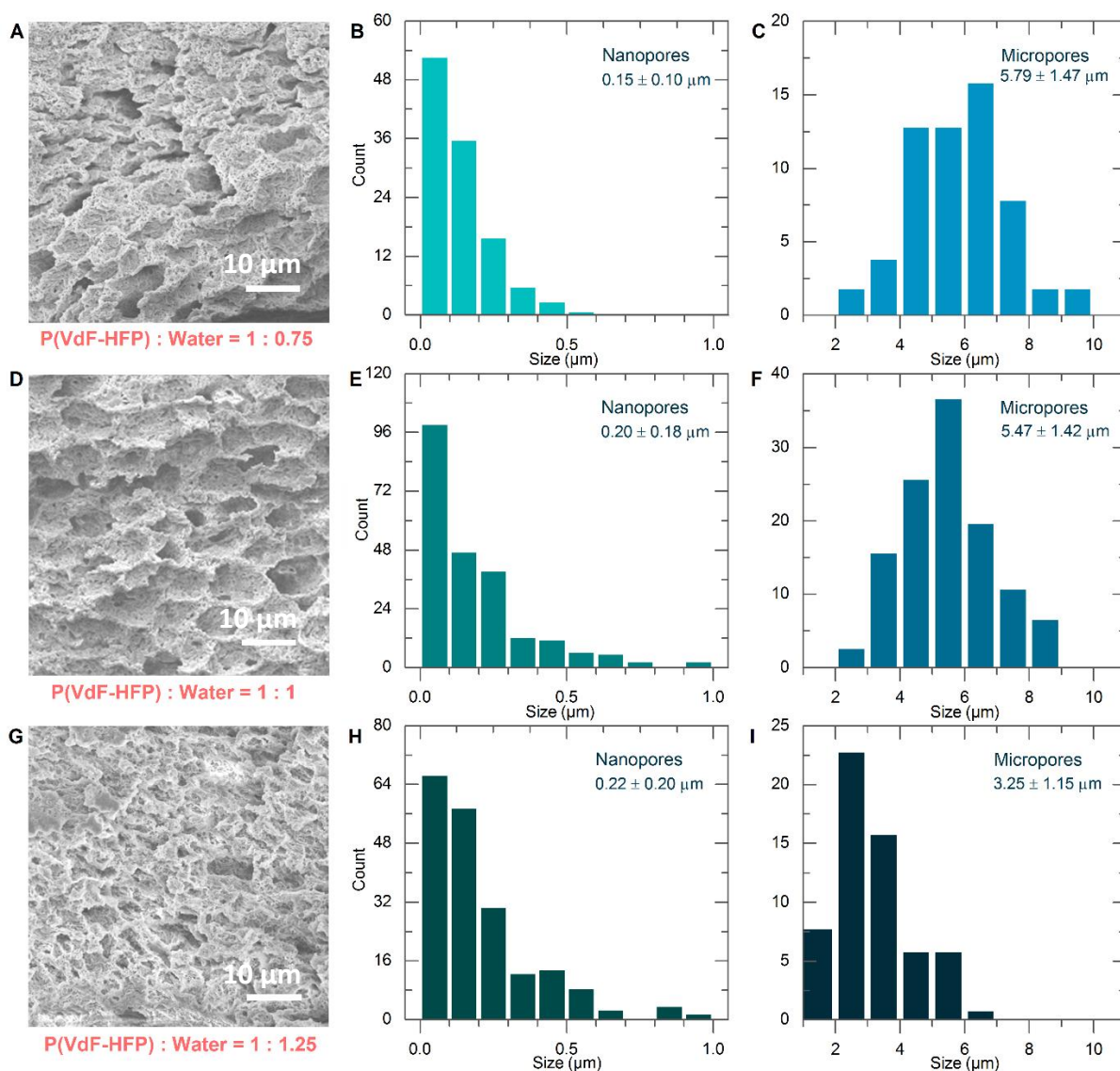
**Figure S5.** (A) Pore number distribution of P(VdF-HFP)<sub>HP</sub> measured by USAXS technique, showing the hierarchically porous structure. (B) Raw data from USAXS. (C) Pore volume distribution comparing SEM and micro-CT measurements.

To demonstrate that the morphology of P(VdF-HFP)<sub>HP</sub> is reproducible by our phase-inversion based fabrication process, multiple samples were made using the standard precursor solution (containing a P(VdF-HFP):Acetone:Water mass ratio of 1:8:1), and micrographed. The results are shown in Fig. S6. Evidently, the samples are all hierarchically porous, and pore size measurements indicate that both the nanopore and micropore size distributions are similar across the samples. While there are small sample-to-sample variations (not statistically significant, and attributable to the sampling and inherently random nature of the thermodynamic phase-inversion process), the results indicate that the hierarchically porous structure is reproducible by the phase-inversion technique.



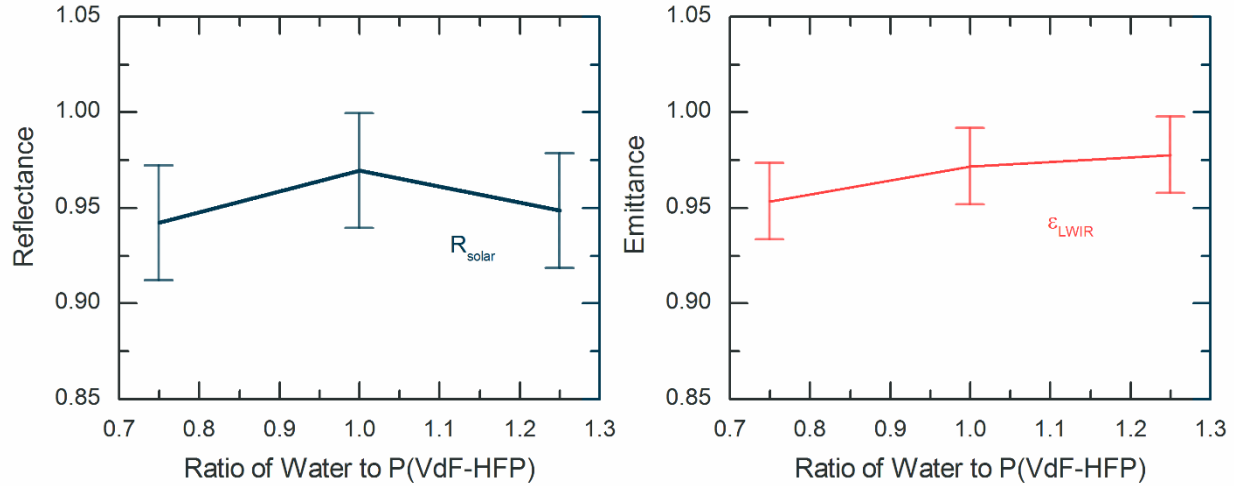
**Figure S6.** (A-C) SEM Micrographs of three different samples of P(VdF-HFP)<sub>HP</sub>, (D-E) corresponding nanopore size distributions and (G-I) corresponding micropore size distributions.

The morphology of phase-inverted porous polymers depends on several factors, such as polymer : solvent : nonsolvent ratio in the precursor, type of solvent or nonsolvent, and the rate of decrease in solvent concentration (32, 33). These factors have been widely used to control the morphology for desalination membranes (32). In this investigation, we varied the polymer : nonsolvent ratio and investigated its effects on the morphology. Fig. S7 shows representative SEM micrographs and pore size measurements. As shown, the nanopore size distributions (Figs. S7B, E and H) show no discernible trend even though the amount of water changes by 50% relative to the amount of P(VdF-HFP). However, it is clear from the SEM images in Figs. S7A, D and G, that a P(VdF-HFP) : Water ratio of 1:1.25 produces much smaller pores compared to 1:1 and 1:0.75 ratios. This is reflected in the micropore size distributions, which are similar for ratios of 1:0.75 and 1:1 (Figs. S7C and F, showing mean pore sizes of  $\sim 5.8$  and  $\sim 5.5$   $\mu\text{m}$  respectively), but show a downward shift for a ratio of 1:1.25 (Fig. S7I, showing a mean pore size  $\sim 3.3$   $\mu\text{m}$ ).



**Figure S7.** (A) SEM image, (B) nanopore size distribution and (C) micropore size distribution for P(VdF-HFP):Water ratio of 1:0.75. (D-F) Corresponding data for a 1:1 ratio and (G-I) for a 1:1.25 ratio.

Although the results in Fig. S7 suggests that the morphology of P(VdF-HFP)<sub>HP</sub> is tunable by changing the composition of the precursor solution, optical measurements of samples made with the above P(VdF-HFP):Water ratios show that  $\bar{R}_{solar}$  and  $\epsilon_{LWIR}$  does not change significantly even though the amount of water relative to P(VdF-HFP) changes by 50% (Fig. S8). From an optical perspective, this is expected, as the tested P(VdF-HFP):Water ratios all yield a wide range of small and large pores (with a size range of  $\sim 200$  nm to  $6\text{ }\mu\text{m}$  or greater) that together scatter all solar wavelengths efficiently. However, it also shows that the phase-inversion technique can be a robust manufacturing method, as it yields high optical performance without much finesse.

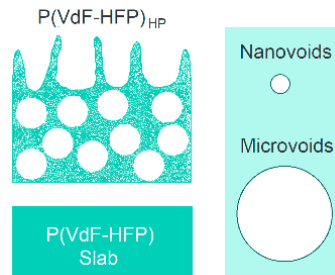


**Figure S8.** Solar reflectances and thermal emittances of P(VdF-HFP)<sub>HP</sub> samples made using different P(VdF-HFP):Water ratios. Error bars indicate the uncertainty in measurements. Evidently, the performance shows no significant changes even though the amount of water is changed by 50% relative to the amount of P(VdF-HFP).



## Section 6. Finite-Difference-Time-Domain Simulations

To investigate the effect the hierarchical porous structure has on  $P(\text{VdF-HFP})_{\text{HP}}$ 's optical properties, Finite-Difference Time-Domain (FDTD) simulations were carried out using FDTD Solutions 8.6.1 software by Lumerical. Due to computational constraints, two dimensional models were used. For the solar wavelengths (0.35-2.5  $\mu\text{m}$ ), scattering cross sections of circular voids of different sizes (Fig. S9) in  $P(\text{VdF-HFP})$  were simulated using a total-field scattered-field source. As shown in Fig. 2D, microvoids of sizes  $\sim 5 \mu\text{m}$  efficiently scatter sunlight regardless of the wavelength, whereas the nanovoids  $\sim 0.2 \mu\text{m}$  in size selectively scatter UV and visible wavelengths. In a sufficiently thick  $P(\text{VdF-HFP})_{\text{HP}}$  layer, both micro- and nano-voids are present in abundance and contribute to the reflectance. Consequently, the spectral reflectance is  $R(\lambda)$  is  $\gtrsim 0.95$  even at the longer solar wavelengths, and only rises towards the blue end of the spectrum (Fig. 1D).



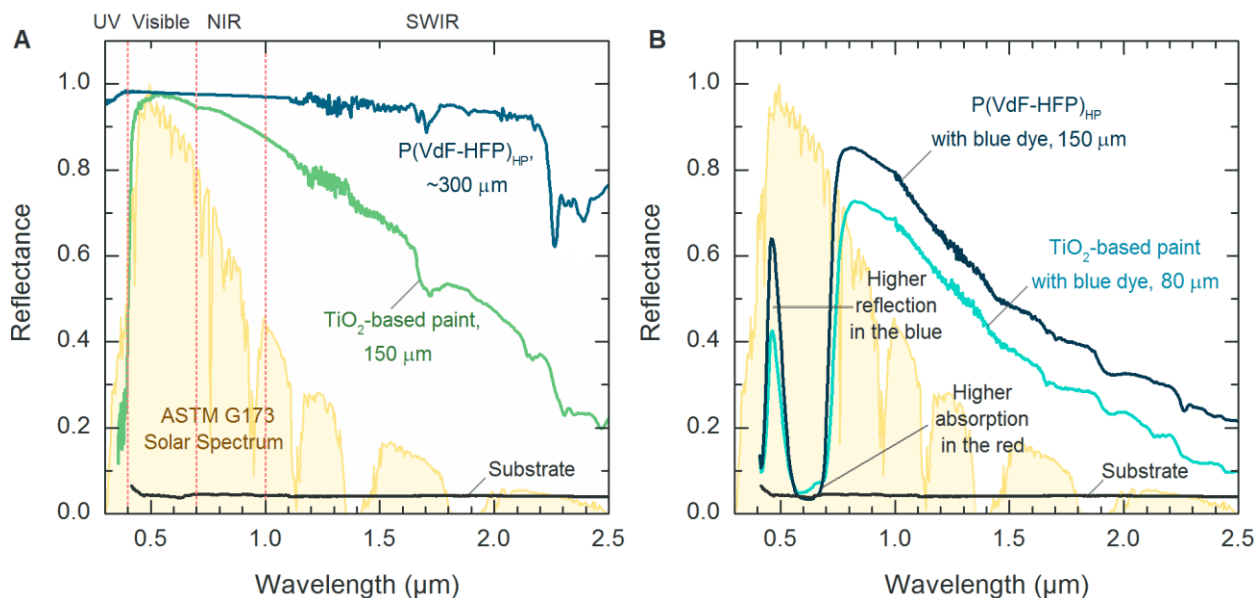
**Figure S9.** Graphical renditions of the structures used for the FDTD simulations.

In the LWIR wavelengths (8-13  $\mu\text{m}$ ), spectral reflectance  $R(\lambda)$  for light incident at various angles from the air above were simulated for semi-infinite solid slabs and hierarchically porous  $P(\text{VdF-HFP})$  coatings. For  $P(\text{VdF-HFP})_{\text{HP}}$ , which was experimentally measured to be 50% porous, it was assumed that both the microporosity and the nanoporosity (Section 5) of the matrix around the microvoids were 29.2% (i.e.  $1 - \sqrt{0.5}$ ). Since the nanovoids ( $\sim 50\text{-}100 \text{ nm}$  size) are much smaller than the LWIR wavelengths, the nanoporous phase was represented by a Maxwell-Garnett effective medium. The microvoids, on the other hand, were represented by  $10 \mu\text{m}$  circular voids randomly dispersed in the nanoporous phase (Fig. S9). Lastly, to mimic the open, porous surface of the  $P(\text{VdF-HFP})_{\text{HP}}$ , the surface features were represented by exclusions of randomly varying sizes  $\sim 10 \mu\text{m}$  on the top surface (Fig. S9).

As evident from Fig. 2E, the simulated spectral emittance  $\epsilon(\lambda) = 1 - R(\lambda)$  of the modelled  $P(\text{VdF-HFP})_{\text{HP}}$  is higher than that of the solid  $P(\text{VdF-HFP})$  slab. This indicates that the open, porous surface and the effective medium behavior of the nanoporous phase leads to a gradual refractive index transition across the polymer-air interface in the LWIR wavelengths. This reduces the surface reflectance and results in a high  $\epsilon(\lambda)$ . The effective medium behavior also lowers the refractive index contrast between the nanoporous phase and the microvoids, reducing any backscattering from the microvoids that might raise  $R(\lambda)$  and lower  $\epsilon(\lambda)$ . Overall, the two effects result in a consistently higher  $\epsilon(\lambda)$  for  $P(\text{VdF-HFP})_{\text{HP}}$  compared to a solid slab. As shown in Fig. 2F, this also leads to a higher  $\bar{\epsilon}_{\text{LWIR}}(\theta)$  for  $0^\circ$  to  $80^\circ$  angles of emission for  $P(\text{VdF-HFP})_{\text{HP}}$ , allowing it to exhibit a high hemispherical  $\bar{\epsilon}_{\text{LWIR}}$ .

## Section 7. Comparison with a Commercial White Paint

Fig. S10A shows the spectral reflectances of a P(VdF-HFP)<sub>HP</sub> coating with thickness  $\sim 300\ \mu\text{m}$  (effectively  $\sim 150\ \mu\text{m}$ , as mentioned in Section 3) and a TiO<sub>2</sub>-based commercial white paint (Sherwin Williams, 636613 High Reflective White) coating with thickness  $\sim 150\ \mu\text{m}$ . As shown, the TiO<sub>2</sub>-based paint shows a sharp drop in reflectance for bluer wavelengths  $< 0.45\ \mu\text{m}$  due to the intrinsic absorption of the TiO<sub>2</sub>. Crucially, the reflectance drops to  $\sim 0.2$  in the UV, which contains about 6% of sunlight. This implies that TiO<sub>2</sub>-based paints have a theoretical maximum  $\sim 0.95$  for  $\bar{R}_{\text{solar}}$ . The reflectance of the TiO<sub>2</sub>-based paint also drops in the longer, NIR-to-SWIR wavelengths ( $0.7\text{--}2.5\ \mu\text{m}$ ), likely because the TiO<sub>2</sub> particles in the paint are too small to effectively scatter such wavelengths. In contrast, the P(VdF-HFP)<sub>HP</sub> coating has very little absorption in the ultraviolet to blue wavelengths, and the presence of both small ( $\sim 0.2\ \mu\text{m}$ ) and large ( $\sim 5\ \mu\text{m}$ ) pores in it means all solar wavelengths are efficiently scattered to result in a high  $\bar{R}_{\text{solar}}$  (0.96 in this case, as opposed to 0.86 for the TiO<sub>2</sub>-based paint). A similar result is seen for a blue variant (Fig. S10B), where a blue P(VdF-HFP)<sub>HP</sub> coating (thickness  $150\ \mu\text{m}$ , effectively  $\sim 75\ \mu\text{m}$ ) shows a higher  $\bar{R}_{\text{NIR-SWIR}}$  (0.67) than a  $80\ \mu\text{m}$  thick TiO<sub>2</sub>-based paint coating (0.54) colored with the same dye. In fact, P(VdF-HFP)<sub>HP</sub> appears to yield a more vivid color, with a higher reflectance in the blue and higher absorbance in the red wavelengths observed relative to the TiO<sub>2</sub>-based paint.



**Figure S10.** Reflectance spectra across the solar wavelengths of (A) a P(VdF-HFP)<sub>HP</sub> coating (thickness  $\sim 300\ \mu\text{m}$ , effectively  $\sim 150\ \mu\text{m}$  accounting for the porosity), and of a TiO<sub>2</sub>-based commercial white paint (Sherwin Williams, 636613 High Reflective White, thickness  $150\ \mu\text{m}$ ). (B) Analogues that were dyed blue. Reflectance of the black substrates ( $R_{\text{solar}}(\lambda) \sim 0.05$ ) for the coatings is also shown.

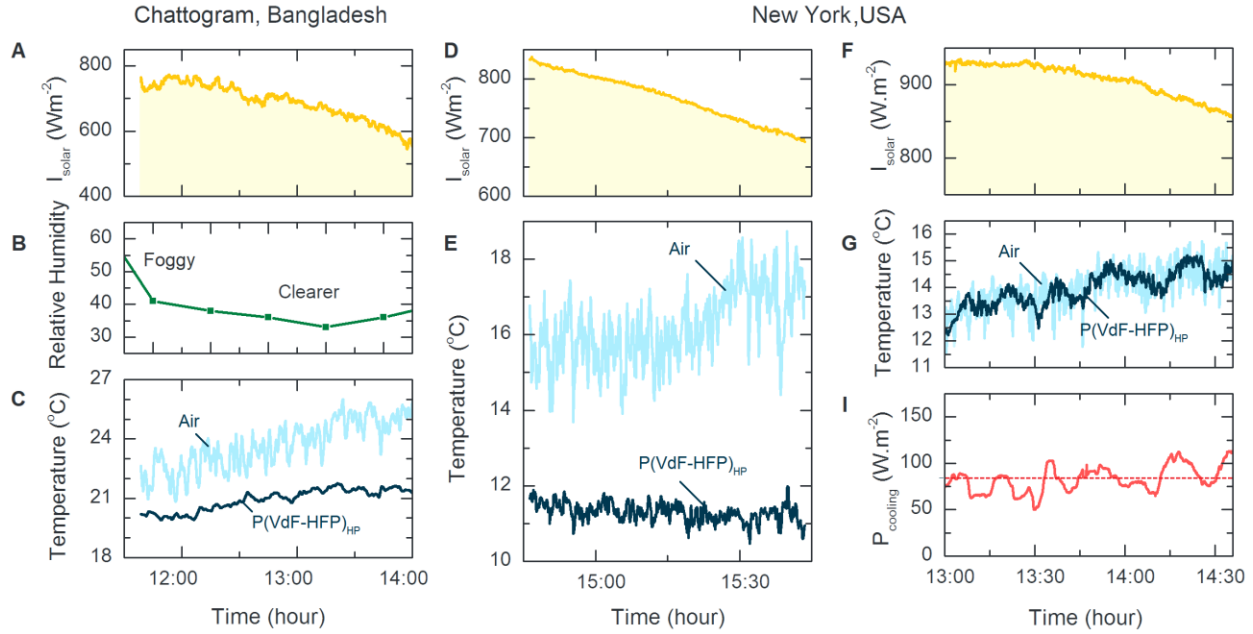
## Section 8. Demonstration of Cooling Power and Sub-ambient PDRC Performance

Demonstrations of the cooling performance of the P(VdF-HFP)<sub>HP</sub> coatings were carried out under clear skies in Phoenix, Arizona on March 03, 2018 over a 30-minute period and New York, USA on March 31, 2018 over a 1.5-hour period. Since  $P_{cooling}$  is entirely dependent on radiative heat transfer (Equation S3), it was measured as the power required to balance the radiative heat loss from the coatings and keep them at the ambient temperature (and make convective and conductive heat transfer much smaller than the radiative losses) under an open sky. Sub-ambient PDRC performance was also measured in Phoenix and New York on the same days. An additional measurement of sub-ambient PDRC performance was taken under foggy skies in Chattogram, Bangladesh, on January 10, 2018. Location and meteorological data are provided later in the section.

Fig. 3A of the main text shows the setup. As shown, we opted to completely expose the P(VdF-HFP)<sub>HP</sub> coatings to the ambient air. This was done because firstly, encasing the P(VdF-HFP)<sub>HP</sub> in a convection shielding box can set up temperatures and microclimates that differ from that of the ambient air. Secondly, materials typically used for convection shield also block the passage of sunlight and thermal radiation by optical interference or by absorption (for example, poly(ethene) films which are commonly used, absorb ultraviolet light and some infrared wavelengths). An exposed configuration would thus yield a truer value for  $P_{cooling}$ . An aluminum foil-coated cardboard box was used as a radiation shield around the P(VdF-HFP)<sub>HP</sub> sample, to block nearby tall buildings and the rest of the experimental setup from its field of view.

For the cooling power tests, the P(VdF-HFP)<sub>HP</sub> sample consisted of a 15 cm x 15 cm x 300- $\mu$ m P(VdF-HFP)<sub>HP</sub> coating on a 15 cm x 15 cm x 1-mm thick copper sheet. The other face of the copper sheet was attached to a 15 cm x 15 cm heating strip atop a 15 cm x 15 cm x 5 cm Styrofoam block and connected to a computer-controlled voltage supply. Two thermocouples were placed between the P(VdF-HFP)<sub>HP</sub> coating and the copper sheet to measure the coating's temperature. Thermocouples were also placed around the sample to measure the ambient temperature. The ensemble was then placed in the radiation shielding box and left outdoors (on a field in Phoenix and on rooftops in New York and Chattogram), with the temperature of the air and the P(VdF-HFP)<sub>HP</sub> coating fed into a feedback-control program that adjusted the voltage supplied to the heater to maintain the coating at ambient temperature. A pyranometer (Apogee, SP 510) connected to the computer was used to simultaneously measure the hemispherical  $I_{solar}$ . For the sub-ambient PDRC demonstration, the heater was switched off, and the temperatures of the air, the P(VdF-HFP)<sub>HP</sub> coating and  $I_{solar}$  recorded over a period of time. The measured cooling powers and sub-ambient temperatures are presented in Fig. 3 of the main text and Fig. S11 of the Supplementary information.



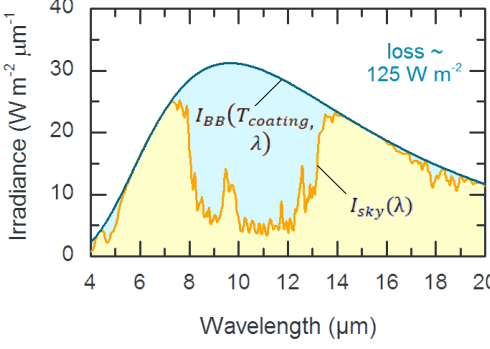
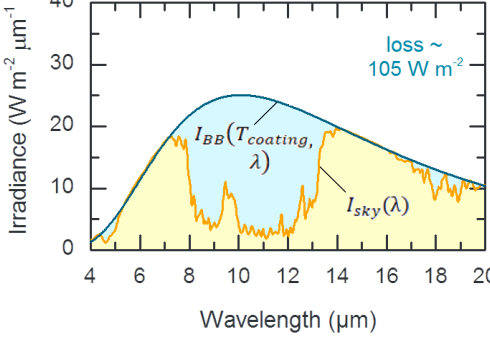


**Figure S11.** (A) Solar intensity, (B) humidity and (C) temperatures of the air and P(VdF-HFP)<sub>HP</sub> sample in Chattogram, Bangladesh. As shown, with a drop in solar intensity and the clearing of the fog (indicated by the lowering of the humidity) (34), the temperature difference between the sample and air increases. (D) Solar intensity and (E) temperatures of the air and P(VdF-HFP)<sub>HP</sub> sample in New York, USA. (F) Solar Intensity, (G) air and sample temperatures and (H) cooling power observed in New York, USA. Dotted line indicates the average  $P_{cooling}$  over the period of the experiment.

As shown in Figs. 3E and H and S11C, E and G, the temperature of the air fluctuated considerably during the measurements, often by as much as 3-4°C within the span of a minute. The fluctuations arise from sudden wind gusts (estimated to be between 1-3 m s<sup>-1</sup> from observations of small pieces of paper released into the wind) that bring about local changes in ambient temperature. Nonetheless, for  $P_{cooling}$  measurements, the temperature of the P(VdF-HFP)<sub>HP</sub> coating closely followed that of the air (Figs. 3H and S11G). Given the close match between the coating and air temperature, convective heat transfer is small compared to the radiative loss, making the average  $P_{cooling}$  over the duration of the experiments (83 W m<sup>-2</sup> for New York and 96 W m<sup>-2</sup> for Phoenix (Fig. 3F) reliably accurate.

The measured cooling powers are consistent with  $P_{cooling}$  predicted by simplified MODTRAN 6 infrared radiance models of the sky and the assumption that  $\bar{R}_{solar} = 0.96 \pm 0.02$  and  $\bar{\epsilon}_{LWIR} = 0.97$  for the P(VdF-HFP)<sub>HP</sub> coatings used. As shown in Table S1,  $P_{cooling}$  was predicted at  $69 \pm 18$  W m<sup>-2</sup> in New York and  $95 \pm 15$  W m<sup>-2</sup> in Phoenix for the tests. Since  $I_{solar}$  was moderately high during the tests (Table S1), the uncertainty of  $\pm 0.02$  in  $\bar{R}_{solar}$  alone accounts for the difference between the measured and predicted  $P_{cooling}$  values. Therefore, even without considering uncertainties in the estimated thermal emission, the measured and predicted  $P_{cooling}$  values for P(VdF-HFP)<sub>HP</sub> coatings are consistent with each other. Discussions of additional uncertainties in predicted  $P_{cooling}$  are presented in Section 9.

**Table S1.** Estimated cooling powers of the P(VdF-HFP)<sub>HP</sub> coatings during the tests in Phoenix and New York.

Location	Parameters	$I_{BB}(T_{coating}, \lambda)$ , $I_{sky}(\lambda)$ and radiative loss from P(VdF-HFP) <sub>HP</sub>	$P_{cooling}$ with $\bar{R}_{solar} = 0.96 \pm 0.02$ ( $W m^{-2}$ )
<b>Phoenix, AZ</b>	<ul style="list-style-type: none"> <li>Midlatitude, arid, Summer.</li> <li>Location: 33.3837°N, 112.0528°W</li> <li>Elevation: 349 m</li> <li>Time: 2018-03-03, 15:00 local time</li> <li>Air temperature ~26.5°C</li> <li>Total precipitable water ~7 mm (35)</li> <li>Sky Clear, Visibility 16.1 km (34)</li> <li><math>I_{solar} \sim 745 W m^{-2}</math> (direct normal ~1085 <math>W m^{-2}</math>, diffuse ~69 <math>W m^{-2}</math>).</li> <li>Wind: Periodic, 1-2 <math>m s^{-1}</math>.</li> </ul>		$95 \pm 15$
<b>New York, NY</b>	<ul style="list-style-type: none"> <li>Midlatitude, coastal. Winter.</li> <li>40.8905°N, 73.9106°W</li> <li>Elevation 85 m</li> <li>Time: 2018-03-31, 13:30 local time</li> <li>Air temperature ~14.5°C</li> <li>Total precipitable water ~5 mm (35)</li> <li>Sky Clear, Visibility 16.1 km (34)</li> <li><math>I_{solar} \sim 901 W m^{-2}</math> (direct normal ~1017 <math>W m^{-2}</math>, diffuse ~67 <math>W m^{-2}</math>).</li> <li>Wind: Periodic, 1-3 <math>m s^{-1}</math>.</li> </ul>		$69 \pm 18$

From Figs. 3E and S11C and E, it is clear that when the P(VdF-HFP)<sub>HP</sub> coatings were not actively heated, they exhibited remarkable sub-ambient temperatures even without the use of convection shields. A drop  $\Delta T$  of ~6°C was observed in the warm, arid conditions of Phoenix (Fig. 3E), while a  $\Delta T \sim 5^\circ C$  was seen in a cold afternoon in New York (Fig. S11E). Remarkably, even under a foggy and hazy winter sky in the tropical and coastal region of Chattogram (22.3612°N, 91.8371°E, Elevation: 56 m, Date: 2018-01-10, 12:30, Air temperature ~24° C, Visibility 3.2 km, Total precipitable water ~10 mm) (34, 36), a  $\Delta T \sim 3^\circ C$  was observed (Fig. S11C). The high sub-ambient cooling performances under a wide variety of conditions and without any convection shields highlights the superb PDRC capability of the P(VdF-HFP)<sub>HP</sub> coatings, and makes them attractive for use.


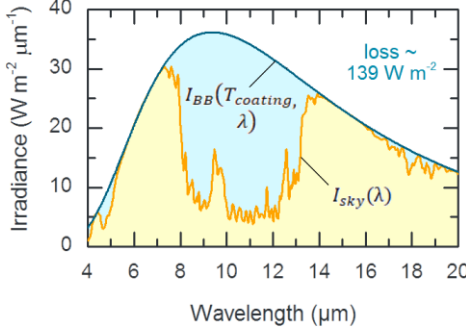

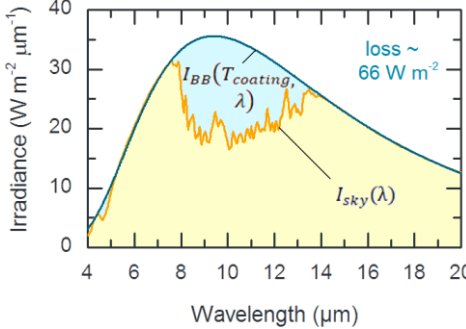
## Section 9. Theoretical Estimation of Cooling Powers Under Two Different Summertime Skies

While a sufficiently high  $\bar{R}_{solar}$  and  $\bar{\epsilon}_{LWIR}$  can help a passive daytime radiative cooler achieve a net heat loss or  $P_{cooling}$ , the magnitude of  $P_{cooling}$  depends greatly on variables that determine the total solar intensity  $I_{solar}$  and the sky's hemispherical spectral radiance  $I_{sky}(\lambda)$ . For instance, higher solar elevation angles, lower surface temperatures, lower elevations (i.e. thicker atmospheres), higher humidities and higher aerosol contents lead to a low  $P_{cooling}$  (21, 22). Consequently, a subtropical and humid location like South Asia should see lower  $P_{cooling}$  than a mid-latitude, arid and elevated location like Arizona, USA. However, unlike  $I_{solar}$ , which can be conveniently measured with a pyranometer,  $I_{sky}(\lambda)$  is difficult to measure. Therefore, for this investigation, we used weather and location data to model  $I_{sky}(\lambda)$  for different sites using the MODTRAN® 6 Web Application. Parameters used for the modelling included location, time and total precipitable water in the atmosphere (TPW). A clear, cloudless sky was assumed. The resulting  $I_{sky}(\lambda)$  was scaled to represent the local ambient temperature ( $= T_{coating}$ ) (21).  $P_{cooling}$  was then calculated using available or estimated  $I_{solar}$  using Equation S3 and assuming  $\bar{R}_{solar} = 0.96 \pm 0.02$  and  $\bar{\epsilon}_{LWIR} = 0.97$ .

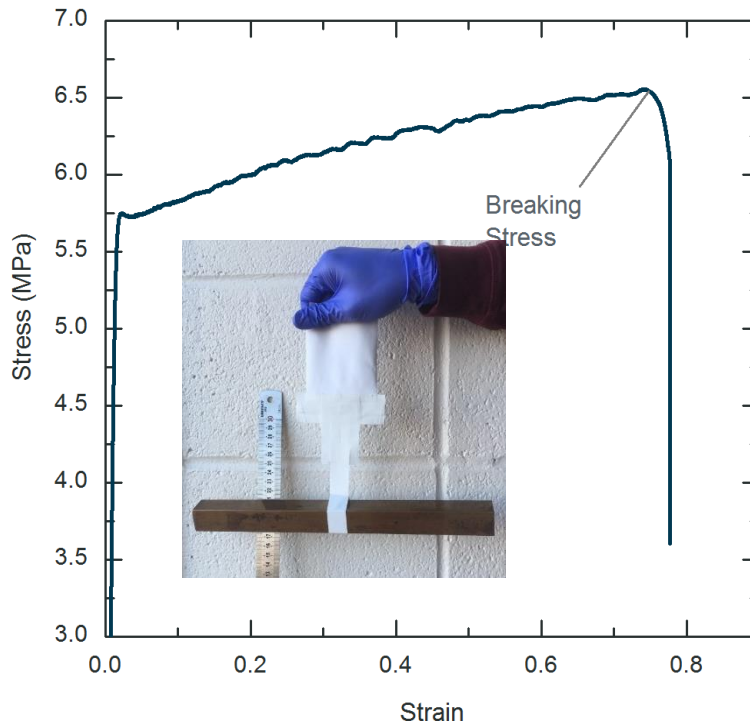
The predicted  $P_{cooling}$  for the test locations and dates are presented in Section 8, Table S1, and are consistent with measured values. In this section, we further explore the cooling potential of P(VdF-HFP)<sub>HP</sub> coatings during peak summer noontimes in an arid (Southwestern USA) and a humid (South Asia) location. For each location, a cloudless sky with solar intensity (ASTM G173 Global Spectrum), adjusted for noon-time solar zenith angle is assumed, and the average noon-time weather data for the hottest week in 2017 is used. The results are shown in Table S2. Evidently, P(VdF-HFP)<sub>HP</sub> coatings can achieve cooling even under strong sunlight and contrasting climates during the summer. However, humidity or total precipitable water (TPW) heavily influences the magnitude of  $P_{cooling}$ . As the blue region ( $I_{BB}(T_{coating}, \lambda) - I_{sky}(\lambda)$ ) of the infrared spectral radiance graphs for the two locations indicate, the cooling power can vary by  $\sim 70$  for  $W m^{-2}$  for large variations in TPW. The reduced heat loss for high TPWs means that for humid locations such as South Asia, a near-perfect  $\bar{R}_{solar}$  is crucial. As discussed earlier, cool roof paints fall well-short in this regard (Section 7) and would heat up, but P(VdF-HFP)<sub>HP</sub>, which can attain  $\bar{R}_{solar} > 0.98$  for thickness  $> 480 \mu m$ , could still achieve cooling in such situations (Fig. S11C).

It should be noted that the atmospheric radiances presented are approximations. For instance, they do not account for the reduction in  $I_{solar}$  due clouds, which become likelier with rising TPW.  $P_{cooling}$  is thus likely to be higher than estimated for South Asia, which often sees cloudy skies during the summer. Furthermore, the calculation of  $I_{sky}(\lambda)$  is based on a simplified model that does not account for variations in the distribution of water vapor through the height of the atmosphere (e.g. a low-lying warm fog would impede radiative heat loss much less if instead it was distributed as a cold cloud high above) (21). Lastly, the models also rely on low-resolution meteorological data that might deviate from the exact weather in the test locations (28, 29). For instance, a small error of 2 mm in TPW can change  $P_{cooling}$  by  $5 W m^{-2}$ . With even larger uncertainties arising from the  $\pm 0.02$  variation in  $\bar{R}_{solar}$ , differences of  $\sim 20 W m^{-2}$  between theoretical and measured values are to be expected.

**Table S2:** Estimated noon-time cooling powers of the P(VdF-HFP)<sub>HP</sub> coatings during peak summer in Southwest USA and South Asia.

Location	Parameters	$I_{BB}(T_{coating}, \lambda)$ , $I_{sky}(\lambda)$ and radiative loss from P(VdF-HFP) <sub>HP</sub>	$P_{cooling}$ with $\bar{R}_{solar} = 0.96 \pm 0.02$ ( $W m^{-2}$ )
<b>Southwestern USA</b> 	<ul style="list-style-type: none"> <li>▪ <b>Midlatitude arid desert, hot summer</b></li> <li>▪ Time: Late-May, noon</li> <li>▪ Temperature <math>\sim 36^{\circ}C</math> (34)</li> <li>▪ Total precipitable water <math>\sim 9</math> mm (35)</li> <li>▪ Elevation <math>\sim 300</math> m.</li> <li>▪ Solar elevation <math>\sim 76.3^{\circ}</math> <ul style="list-style-type: none"> <li>• <math>I_{solar} \sim 990 W m^{-2}</math></li> </ul> </li> </ul>		$99 \pm 20$
<b>South Asia</b> 	<ul style="list-style-type: none"> <li>▪ <b>Subtropical, humid summer</b></li> <li>▪ Time: Mid-May, noon</li> <li>▪ Temperature <math>\sim 35^{\circ}C</math> (34)</li> <li>▪ Total precipitable water <math>\sim 32</math> mm (35)</li> <li>▪ Elevation <math>\sim 300</math> m</li> <li>▪ Solar elevation <math>\sim 80.3^{\circ}</math> <ul style="list-style-type: none"> <li>• <math>I_{solar} \leq 1000 W m^{-2}</math> (due to clouds.)</li> </ul> </li> </ul>		$26 \pm 20$ (likely higher due to clouds)

## Section 10. Mechanical Strength and Recyclability of Freestanding P(VdF-HFP)<sub>HP</sub> sheets

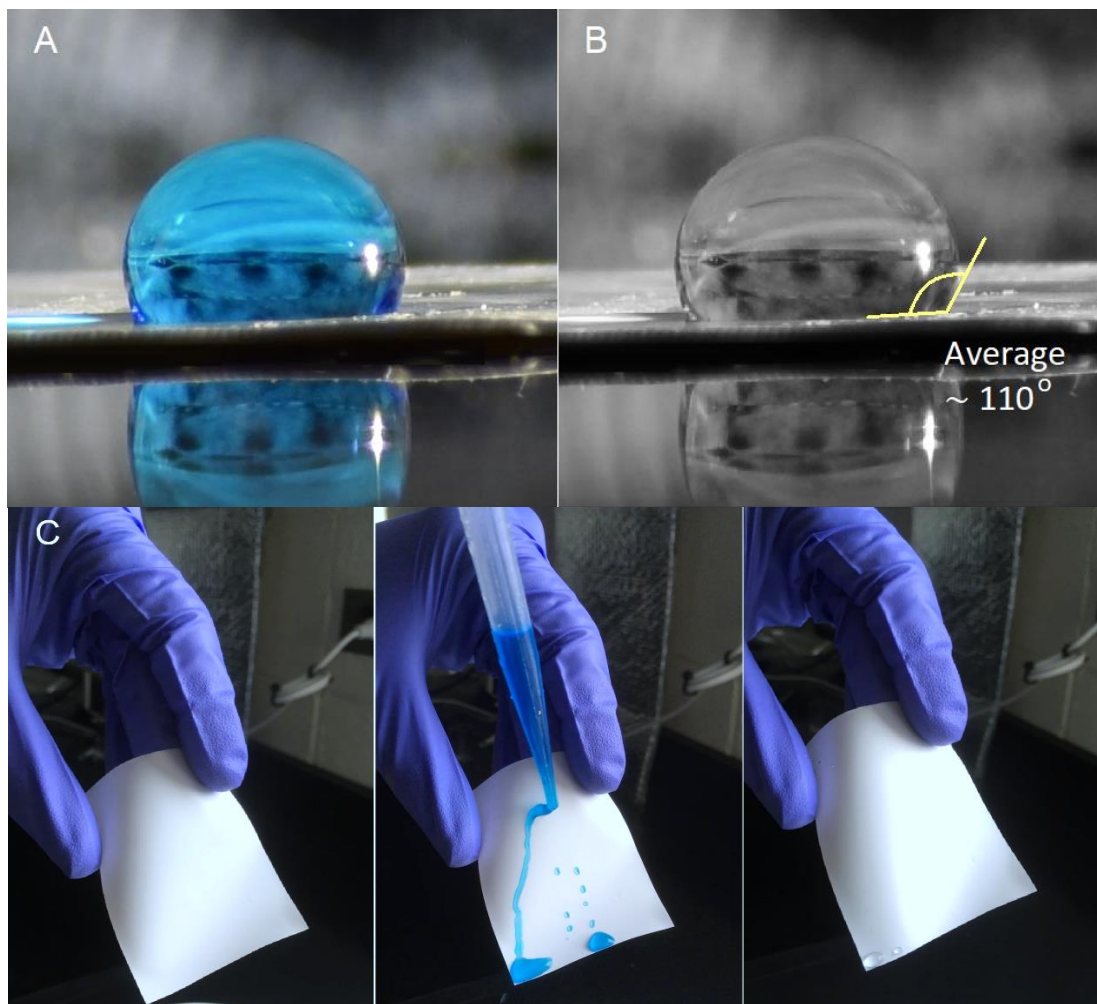


**Figure S12.** Stress-strain curve for a 200  $\mu\text{m}$  thick P(VdF-HFP)<sub>HP</sub> sheet. The breaking stress of 6.6 MPa corresponds to the weight of a 630 m long sheet of the same width and thickness. Inset shows a free-standing P(VdF-HFP)<sub>HP</sub> sheet of 72 mm width and 200  $\mu\text{m}$  thickness supporting a copper block weighing 1.77 kg. As indicated by the measurements, the mechanical strength of the P(VdF-HFP)<sub>HP</sub> is clearly suitable for tarpaulin-like designs.



**Figure S13.** Due to their all-polymer composition, dirty, free-standing P(VdF-HFP)<sub>HP</sub> sheets or peeled coatings can be easily recycled by re-dissolving the sheets in a P(VdF-HFP)-acetone-water precursor solution, letting any dirt settle, and making pristine coatings from the clear solution on top. This promising recyclability is an added benefit to its already green and energy-saving functionality. Indeed, given the variety of phase-inversion-compatible polymers shown in Section 13, the phase inversion process might create new avenues for recycling waste plastics to make structured polymer PDRC coatings.

## Section 11. Hydrophobicity and water repelling behavior



**Figure S14.** (A) Photograph of a dyed water droplet on a P(VdF-HFP)<sub>HP</sub> coating. (B) Contact angle for the droplet – the average value is 110°. (C). Photographs of a P(VdF-HFP)<sub>HP</sub> coating showing its appearance before, during and after wetting with dyed water. No changes are observed, even after 5 mins of wetting, which indicates the water resistance and potentially self-cleaning behavior of the coating.

## Section 12. Aging and Exposure Tests

Several different stability tests were conducted on pieces of P(VdF-HFP)<sub>HP</sub> coatings on plastic. Prior to the tests, samples were cut in half, with one set of halves kept in a cool, dry environment. After the tests, they were used as references for comparison with the tested samples.

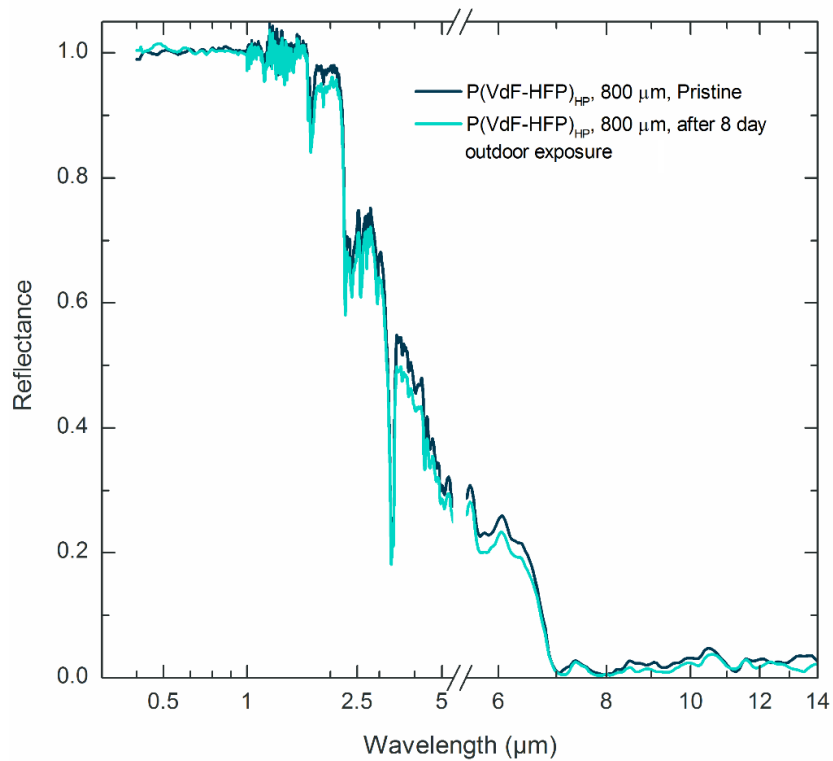
Accelerated thermal aging tests were done by placing one set of ‘half-samples’ in an open glass bottle inside an oven at 80°C for 14 days. An analogous thermal aging test was also done in moist conditions with 100% relative humidity in a closed chamber, with samples observed to be wet during the test. After the tests, samples were taken out and had their reflectances compared against their respective ‘sets of halves’.

To test the effect of prolonged operation in practical conditions, an exposure test under the sky was carried out in New York (40.8101° N, 73.9434° W). ‘Half-samples’ were left close to busy roadside and under winter skies for 30 days (19 November – 18 December, 2017), after which their optical performance was compared to those of their respective pristine halves. An additional 8-day test on thick samples with high  $\bar{R}_{solar}$  and high  $\bar{\epsilon}_{LWIR}$  was also carried out during the summer. Spectral reflectance of the samples before and after the tests are shown in Fig. S15.

Results of the stability tests are presented in Table S3. As shown, accelerated thermal aging under dry and watery conditions has little effect on the optical performance of the coatings. Moreover, coatings exposed to the sky in New York, both for a month during the winter and for 8 days during the summer, stay essentially unchanged. The results are promising, and indicate the durability of P(VdF-HFP)<sub>HP</sub> under different operating conditions.

**Table S3.** Results of the aging and exposure tests carried out on P(VdF-HFP)<sub>HP</sub> coatings.

Test	Description	$\bar{R}_{solar} / \bar{\epsilon}_{LWIR}$	
		Before	After
Accelerated thermal and wet aging tests	80°C in air, for 14 days.	0.95/0.96	0.95/0.96
	80°C in a chamber containing water at 100% relative humidity, for 14 days.	0.96/0.95	0.93/0.96
Monthlong exposure test under the sky in New York	Location: 40.8101° N, 73.9434° W. Date: 19 November – 18 December, 2017. Average Temperature ~5°C, average relative humidity ~65%, occasional rain and light snow.	0.94/0.93	0.93/0.93
	Location: 40.8093° N, 73.9535° W. Date: 09 August – 17 August, 2018. Average Temperature ~25°C, average relative humidity ~75%, occasional rain.	0.996/0.97	0.993/0.98



**Figure S15.** Spectral reflectance of thick (800  $\mu\text{m}$ ) P(VdF-HFP)<sub>HP</sub> samples in their pristine state and after 8-day exposure to the summer sky in New York. As shown the performance of the coatings stay essentially unchanged. The coatings also show the excellent spectral performance – near perfect  $\bar{R}_{\text{solar}}$  and high  $\bar{\epsilon}_{\text{LWIR}}$  achievable by sufficiently thick P(VdF-HFP)<sub>HP</sub> coatings.



### Section 13. Beyond P(VdF-HFP): Phase Inversion as a General Paradigm for Making a Wide Variety of Structured Polymer PDRC Coatings

While the main text demonstrated P(VdF-HFP)-Acetone-Water as one polymer-solvent-nonsolvent system for making PDRC coatings, the phase-inversion based-technique is in fact a generic method for making hierarchical porous polymer coatings with a variety of polymers, solvents and nonsolvents. As a demonstration, coatings made from five additional polymers are shown in Fig. S16. As described below, the choice of these systems is deliberate, and shows that any capability could be incorporated into a structured polymer PDRC coating if a phase-invertible and optically suitable polymer with the required attribute is available. Promisingly, the samples in Fig. S16 show different surface textures, with P(VdF) and PMMA showing matte and glossy appearances respectively. Phase-inversion-based structured polymers are thus versatile like paints in this regard as well.



**Figure S16.** From left to right – samples of structured poly(vinylidene fluoride), poly(methyl methacrylate), poly(styrene), ethyl cellulose and cellulose acetate made by phase inversion on Black foil. The PVdF-Acetone-Water and PMMA-Acetone-Water systems are chosen because variants of the polymers are widely used in the paint industry, and because they yield matte and glossy coatings respectively. The poly(styrene)-tetrahydrofuran-water system is chosen because of poly(styrene)’s suitability for high-temperature (> 200°C) PDRC coatings. The ethyl cellulose-ethanol-water system is chosen to show a completely biocompatible and biodegradable variant, and the cellulose acetate-acetone-water system is chosen to show the compatibility of bioplastics with the technique.

### References

30. APOC (2018). *AP 256 Elastomeric One Datasheet*. Retrieved from <https://www.apoc.com/pages/technical-data-sheets..>
31. M. U. Vera, D. J. Durian, Angular distribution of diffusely transmitted light. *Physical Review E* **53**, 3215-3224 (1996).
32. A. K. Hołda, I. F. J. Vankelecom, Understanding and guiding the phase inversion process for synthesis of solvent resistant nanofiltration membranes. *Journal of Applied Polymer Science* **132**, n/a-n/a (2015).
33. J. Heo, Y. Choi, K. Y. Chung, J. H. Park, Controlled pore evolution during phase inversion from the combinatorial non-solvent approach: application to battery separators. *Journal of Materials Chemistry A* **4**, 9496-9501 (2016).

34. The Weather Company (2018). *Weather History / Weather Underground*. Retrieved from <https://www.wunderground.com/history/>.
35. A. J. Wimmers, C. S. Velden (2018). *MIMIC-TPW2, CIMSS*. Retrieved from <ftp://ftp.ssec.wisc.edu/pub/mtpw2>.
36. Clean Air and Sustainable Environment Project (2018). *Air Quality Index (AQI) - 10/01/2018*. Retrieved from <http://case.doe.gov.bd/>.